PCCP

View Online
Dynamic Article Links

Cite this: *Phys. Chem. Chem. Phys.*, 2011, **13**, 8733–8746

www.rsc.org/pccp

PAPER

Efficient and robust strong-field control of population transfer in sensitizer dyes with designed femtosecond laser pulses†

Johannes Schneider,[a] Matthias Wollenhaupt,[a] Andreas Winzenburg,[b] Tim Bayer,[a] Jens Köhler,[a] Rüdiger Faust[b] and Thomas Baumert[a]

Received 30th November 2010, Accepted 1st March 2011
DOI: 10.1039/c0cp02723e

We demonstrate control of electronic population transfer in molecules with the help of appropriately shaped femtosecond laser pulses. To this end we investigate two photosensitizer dyes in solution being prepared in the triplet ground state. Excitation within the triplet system is followed by intersystem crossing and the corresponding singlet fluorescence is monitored as a measure of population transfer in the triplet system. We record control landscapes with respect to the fluorescence intensity on both dyes by a systematic variation of laser pulse shapes combining second order and third order dispersion. In the strong-field regime we find highly structured topologies with large areas of maximum or minimum population transfer being insensitive over a certain range of applied laser intensities thus demonstrating robustness. We then compare our experimental results with simulations on generic molecular potentials by solving the time-dependent Schrödinger equation for excitation with shaped pulses. Control landscapes with respect to population transfer confirm the general trends from experiments. An analysis of regions with maximum or minimum population transfer indicates that coherent processes are responsible for the outcome of our excitation process. The physical mechanisms of joint motion of ground and excited state wave packets or population of a vibrational eigenstate in the excited state permit us to discuss the molecular dynamics in an atom-like picture.

1. Introduction

Coherent control is a fascinating facet of femtochemistry.[1,2] Traditionally femtochemistry deals with laser-based real-time observations of molecular dynamics by making use of light pulses that are short in comparison to the molecular time scale. Coherent control goes beyond this *ansatz*. Here one seeks to actively exert microscopic control over molecular dynamics at the quantum level on intrinsic time scales. The goal is to steer any type of light-induced molecular processes from an initial state to a predefined target state with high selectivity and with high efficiency. Progress in this fast expanding research field is documented in recent text books,[3,4] review articles[5–21] and special issues.[22–25]

Suitable tools to achieve this goal are shaped femtosecond optical laser pulses for which different shaping techniques are reviewed in the literature.[10,26–29] Optimized light fields can be found for example by employing adaptive feedback learning loops[30–36] or by fine tuning the parameters of physically motivated pulse shapes,[37–40] where experimentally determined quantum control landscapes[41–43] can help identifying underlying physical mechanisms especially in the strong-field regime.

In contrast to weak-field (perturbative) quantum control schemes where the population of the initial state is constant during the interaction with the external light field, the strong-field (non-perturbative) regime is characterized by efficient population transfer. Adiabatic strong-field techniques such as rapid adiabatic passage (RAP) or stimulated Raman adiabatic passage[44,45] are employed for instance with laser pulses in the picosecond[10,46–48] to nanosecond domain allowing for population transfer with unit efficiency in quantum state systems. Only recently these techniques were transferred to the femtosecond regime. For example selectivity based on (dynamic Stark-shifted) RAP combined with high efficiency was demonstrated in an atomic ladder system with the help of chirped laser pulses[49] and piecewise adiabatic passage was demonstrated in an atomic two level system with chirped pulse sequences.[50] Furthermore it was shown that effects of dynamic

[a] *Universität Kassel, Institut für Physik und CINSaT, Heinrich-Plett-Str. 40, 34132 Kassel, Germany. E-mail: wollenhaupt@physik.uni-kassel.de, baumert@physik.uni-kassel.de*
[b] *Universität Kassel, Institut für Chemie und CINSaT, Heinrich-Plett-Str. 40, 34132 Kassel, Germany*

† Electronic supplementary information (ESI) available: Video material visualizing laser induced wave packet dynamics (joint wave packet motion or population of a vibrational eigenstate) and population transfer or return for three different types of laser pulses. MALDI-TOF mass spectrum, UV/VIS spectrum and proton NMR spectrum of porphyrazine **1**. See DOI: 10.1039/c0cp02723e

Stark-shift reducing the excitation efficiency can be compensated with temporally structured pulses.[51] Switching electronic population to different final states with high efficiency *via* selective population of dressed states (SPODS) is a further fundamental resonant strong-field effect as the only requirement is intense ultrashort pulses exhibiting time varying phases such as phase jumps[52–55] or chirps.[42,56]

The modification of the electronic potentials due to the interaction with the electric field of the laser pulse has another important aspect pertaining to molecules, as the nuclear motion can be significantly altered in light induced potentials. An experimental review devoted to the topic of small molecules in intense laser fields focusing mainly on H_2^+ excitation and fragmentation dynamics is given in ref. 57. Experimental examples for modifying the course of reactions of neutral molecules after an initial excitation *via* altering the potential surfaces can be found in ref. 58 and 59 where the amount of initial excitation on the molecular potential can be set *via* Rabi type oscillations.[60]

Although a high degree of excitation can be achieved *via* Rabi oscillations, this approach is not attractive for efficient coherent control schemes as the resonant Rabi oscillation period is proportional to the scalar product of the electric dipole moment times the electric field of the laser pulse. As a consequence, different excitation levels are achieved due to the intensity distribution within the focal area of a typical Gaussian laser beam and due to different orientations of the molecules in a typical isotropic sample. This is why the above mentioned adiabatic strong-field approaches are especially important as they are robust to these effects.

Conceptually most of the mechanisms underlying coherent control have been demonstrated in the gas phase. However, as relevant chemistry, biology and medicine are typically taking place in the liquid phase, laser control of dissolved molecules is most promising for applications. The field is reviewed in ref. 15 where direct control of ground state vibrational excitation,[61] control of energy flow in large light harvesting molecules,[62] control of isomerization processes[63,64] and optical discrimination of molecules with nearly identical absorption profiles[65–67] are prominent examples. Examples of robust and efficient electronic excitation of molecules especially in the liquid phase are rare (see ref. 68 and 69 for theoretical discussions).

In this contribution we want to address the latter issue by investigating strong-field excitation of molecules belonging to the class of photosensitizer dyes. Photosensitizer dyes provide a chromophore for interaction with light on the one hand and on the other hand can interact with their chemical environment when reaching the long-lived triplet state by efficient intersystem crossing. The activation of photosensitizer dyes induces generation of reactive oxygen species[70] and by this grants access to a variety of chemical reactions where oxygen is involved.[71] One very promising application of light-activated photosensitizer dyes is in the photodynamic therapy of cancer,[72] especially when chromophore excitation takes place in the transparency window of tissue in the near-infrared range.

Photodynamic therapy with the help of coherent control by femtosecond laser pulses in the strong-field regime could be feasible. Higher order spectral interference excitation with shaped laser pulses has been demonstrated up to a depth of 3 mm in tissue.[73] Strong-field excitation of photosensitizers can be effected up to an applied intensity of 200 GW cm^{-2}, a value that is commonly used as the damage threshold for biological samples.[74] The efficiency of the photodynamic process directly depends on the quantum efficiency of sensitizer triplet formation including the excitation and intersystem crossing step. In strong laser fields one might be able to optimize the sensitizer excitation process or intersystem crossing process. Indication for coherent control of the intersystem crossing rate induced by dynamic Stark-shifts has been found in a theoretical study.[75] Also note within that context, that preliminary results of weak-field control in molecules for photodynamics applications have been recently reported.[76]

The paper is organized as follows. We start in Section 2 with an introduction of the control parameters used in both the experiments and simulations, including the shape and the detuning of the laser pulses. A motivation of the chosen parameters is given along with a mathematical description of the underlying laser electric field. In Section 3 the sensitizer dye experiments are presented in detail with a main focus on the sensitizer dye excitation scheme and the experimental procedure. Numerical simulations of the population transfer in a model molecule are described in Section 4 and are compared with the experimental results. A discussion of our experimental findings as well as an identification of the physical mechanisms at play in the molecular control scheme under study are the subject of Section 5. Section 6 ends the paper with a brief summary and conclusions.

2. Control parameters

In molecular control by shaped ultrashort laser pulses, the choice of appropriate control parameters is crucial to the success of the scenario under study. In the following we motivate three control parameters that have proven relevant in both weak- and strong-field investigations and are used in our experiments.

The first parameter is the static detuning $\delta = \omega_0 - \omega_r$ of the laser central frequency ω_0 with respect to the transition frequency ω_r of the system. In the weak-field regime—besides the fluence—this is the only parameter which is capable of controlling the population transfer for one-photon excitation, since only the overlap of the excitation spectrum with the molecular absorption band determines the final population,[77] being also valid for higher order spectral interferences.[78–81] In the strong-field regime, the detuning for example influences the adiabaticity of light–matter-interaction, having a great effect on population transfer.[44] Experimentally, different detunings δ are examined by studying two different dye molecules with different absorption spectra. Alternatively, tuning of the laser's central frequency while using only one molecule would be an equivalent realization.

The second control parameter is the time dependence of the instantaneous frequency $\omega(t)$ of the laser pulses. It was shown for weak-field excitation of dye molecules that it is possible to follow an excited state wave packet on its potential energy surface energetically by appropriate time dependence of the pulse's instantaneous frequency matching the molecular dynamics.[82–87] In the strong-field regime proper choice of the

instantaneous frequency enables robust population transfer *e.g.* by RAP in level systems[44,45] and also by pump–dump scenarios in dye molecules.[88,89] In this paper we employ linearly chirped (Group Delay Dispersion, GDD) laser pulses to control the time dependence of the instantaneous frequency *via* spectral phase modulation.

The third parameter is introduced to control the time dependence of the field amplitude, *i.e.* the pulse envelope $|\mathscr{E}_{\mathrm{mod}}(t)|$ of a modulated laser pulse. Asymmetric pulses generated by a Third Order Dispersion (TOD) have proven useful for femtosecond material processing[90] and alignment of gas phase molecules.[91] By shifting the maximum field amplitude back and forth in time, Stark-shifts are induced at the required time thus inducing effective population transfer *via* transient resonances. Examples for intensity-induced non-Franck–Condon transitions are known in the literature.[58,59] In this paper we make use of both the time dependence of the instantaneous frequency by GDD and asymmetries of the temporal pulse envelope by TOD.

2.1 Pulse shapes

The pulse shapes resulting from specific spectral modulation functions such as GDD and TOD have been reviewed earlier.[27] To allow for both modulations, controlling instantaneous frequency and pulse asymmetry at the same time, pulses are dispersed by GDD and TOD *simultaneously*. An analytical expression for this class of pulses is derived in order to understand the resulting temporal pulse shapes. To this end we start with the Gaussian shaped pulse envelope with an intensity FWHM (Full Width at Half Maximum) of Δt

$$\mathscr{E}(t) = \mathscr{E}_0 \mathrm{e}^{-\ln(4)\left(\frac{t}{\Delta t}\right)^2}. \tag{1}$$

The light electric field oscillating with the laser carrier frequency ω_0 is

$$E(t) = \mathrm{Re}[\mathscr{E}(t)\mathrm{e}^{\mathrm{i}\omega_0 t}], \tag{2}$$

and the spectrum of the unmodulated field envelope reads

$$\tilde{\mathscr{E}}(\omega) = \varepsilon_\omega \mathrm{e}^{-\ln(4)\left(\frac{\omega}{\Delta\omega}\right)^2}, \tag{3}$$

where the spectral bandwidth of the pulse is $\Delta\omega = \frac{4\ln(2)}{\Delta t}$ and $\varepsilon_\omega = \mathscr{E}_0 \frac{\sqrt{8\pi\ln(2)}}{\Delta\omega}$. The fluence of the pulse is therefore

$$\begin{aligned} \frac{1}{2}\varepsilon_0 cn \int_{-\infty}^{\infty} \mathscr{E}^2(t)\mathrm{d}t &= \frac{1}{4\pi}\varepsilon_0 cn \int_{-\infty}^{\infty} \tilde{\mathscr{E}}^2(\omega)\mathrm{d}\omega \\ &= \frac{1}{4}\varepsilon_0 cn \sqrt{\frac{\pi}{\ln(2)}}\mathscr{E}_0^2 \Delta t, \end{aligned} \tag{4}$$

where ε_0, c and n denote the vacuum permittivity, the speed of light and the refractive index, respectively. Introducing combined spectral phase modulation of the envelope by $\varphi_{\mathrm{GDD}}(\omega) = \frac{1}{2}\phi_2\omega^2$ and $\varphi_{\mathrm{TOD}}(\omega) = \frac{1}{6}\phi_3\omega^3$, we obtain the spectral modulation function

$$\tilde{\mathscr{M}}(\omega) = \mathrm{e}^{-\mathrm{i}\left(\frac{1}{2}\phi_2\omega^2 + \frac{1}{6}\phi_3\omega^3\right)}. \tag{5}$$

The modulated temporal pulse envelope is obtained from the modulated spectrum

$$\tilde{\mathscr{E}}_{\mathrm{mod}}(\omega) = \tilde{\mathscr{E}}(\omega)\tilde{\mathscr{M}}(\omega) \tag{6}$$

by inverse Fourier transform, *i.e.*

$$\begin{aligned} \mathscr{E}_{\mathrm{mod}}(t) &= \frac{1}{2\pi}\int_{-\infty}^{\infty} \tilde{\mathscr{E}}_{\mathrm{mod}}(\omega)\mathrm{e}^{\mathrm{i}\omega t}\mathrm{d}\omega \\ &= \frac{\varepsilon_\omega}{2\pi}\int_{-\infty}^{\infty} \mathrm{e}^{-\ln(4)\left(\frac{\omega}{\Delta\omega}\right)^2}\mathrm{e}^{-\mathrm{i}\left(\frac{1}{2}\phi_2\omega^2 + \frac{1}{6}\phi_3\omega^3\right)}\mathrm{e}^{\mathrm{i}\omega t}\mathrm{d}\omega. \end{aligned} \tag{7}$$

In order to derive an explicit formula for the modulated temporal pulse envelope $\mathscr{E}_{\mathrm{mod}}(t)$ we consider the definition of a scaled Airy function[92]

$$\frac{1}{|\phi|}\mathrm{Ai}\left(-\frac{\tau}{\phi}\right) = \frac{1}{2\pi}\int_{-\infty}^{\infty} \mathrm{e}^{-\mathrm{i}\frac{\phi^3 z^3}{3}}\mathrm{e}^{\mathrm{i}z\tau}\mathrm{d}z. \tag{8}$$

The following substitutions are so chosen as to reproduce the modulated spectrum described in eqn (7)

$$\phi = \sigma(\phi_3)\sqrt[3]{|\phi_3|/2} \tag{9}$$

$$\frac{1}{\varpi^2} = \frac{\ln(4)}{\Delta\omega^2} + \mathrm{i}\frac{\phi_2}{2} \tag{10}$$

$$\tau = t - \frac{2}{\varpi^4\phi_3} \tag{11}$$

$$z = \omega - \mathrm{i}\frac{2}{\varpi^2\phi_3}. \tag{12}$$

In the above equations $\sigma(\phi_3)$ is the signum function, which takes the values ± 1 for $\phi_3 \gtrless 0$. Insertion of these substitutions into eqn (8) and multiplication of both sides of eqn (8) with the factor of

$$\mathrm{e}^{\left(\frac{8}{3\varpi^6\phi_3^2} - \frac{2t}{\varpi^2\phi_3}\right)} \tag{13}$$

reveals the same form as eqn (7). Therefore, the modulated field reads

$$\mathscr{E}_{\mathrm{mod}}(t) = \frac{\varepsilon_\omega}{|\phi|}\mathrm{e}^{\left(\frac{8}{3\varpi^6\phi_3^2} - \frac{2t}{\varpi^2\phi_3}\right)}\mathrm{Ai}\left(-\frac{\tau}{\phi}\right). \tag{14}$$

Writing out the relevant substitutions we arrive at an explicit equation for combined $\phi_2 \equiv$ GDD and $\phi_3 \equiv$ TOD spectral phase modulation

$$\mathscr{E}_{\mathrm{mod}}(t) = \varepsilon_\omega \frac{\mathrm{e}^{\left(\frac{8}{3\varpi^6\phi_3^2} - \frac{2t}{\varpi^2\phi_3}\right)}}{|\phi|}\mathrm{Ai}\left(\frac{\frac{2}{\varpi^4\phi_3} - t}{\phi}\right). \tag{15}$$

Eqn (15) shows that the GDD–TOD-modulated field is a product of an exponential function and an Airy function. However, since ϖ is complex valued due to its contributions $\Delta\omega$ and $\mathrm{i}\phi_2^{-1}$, both the exponential function and the Airy function have in general complex valued arguments. Only if $\phi_2 \to 0$, that is pure TOD modulation, the modulated field

converges to the well-known exponentially damped Airy function.[27]

Using the short hand notation $\mathscr{E} = \mathscr{E}_{\mathrm{mod}}(t)$, it is convenient to derive the temporal phase of the modulated field by

$$\zeta(t) = \arg[\mathscr{E}] = \arctan\left[\frac{\mathrm{Im}(\mathscr{E})}{\mathrm{Re}(\mathscr{E})}\right] \qquad (16)$$

and the instantaneous detuning directly from eqn (15) by

$$\Delta_{\mathrm{opt}}(t) = \dot{\zeta}(t) = \frac{\mathrm{i}}{2}\frac{\mathscr{E}\dot{\mathscr{E}}^* - \dot{\mathscr{E}}\mathscr{E}^*}{\mathscr{E}\mathscr{E}^*}. \qquad (17)$$

Note that introducing the complex bandwidth ϖ defined in eqn (10) provides a general way to obtain explicit equations for combined spectral phase modulation of a Gaussian laser pulse with any given phase function $\varphi(\omega)$ and $\varphi_{\mathrm{GDD}}(\omega)$ in addition.

In Fig. 1 pictorial overview over these shaped pulses is given, considering the four combinations of $\phi_2 = \pm 5000$ fs^2 and $\phi_3 = \pm 200\,000$ fs^3.

The representation of the envelopes $\mathscr{E}_{\mathrm{mod}}(t)$ and the instantaneous detunings $\Delta_{\mathrm{opt}}(t)$ in Fig. 1 indicates that the alternation of the sign of GDD and TOD is reflected in corresponding symmetry operations in the time domain. Because the *temporal* field amplitude and the *temporal* detuning are the physical controls investigated in this contribution, we analyze which symmetry operations on the *spectral* phase function $\varphi(\omega)$ are responsible for the respective *temporal* symmetry operations. To this end, we consider the general case of a phase modulation function decomposed into its *gerade* and *ungerade* contributions $\varphi(\omega) = \varphi_{\mathrm{g}}(\omega) + \varphi_{\mathrm{u}}(\omega)$. Table 1 shows the temporal properties of the field, *i.e.* $\mathscr{E}_{\mathrm{mod}}(t)$ and the instantaneous detuning $\Delta_{\mathrm{opt}}(t)$ for the four possible combinations of sign alternations (conjugations) of the *gerade*

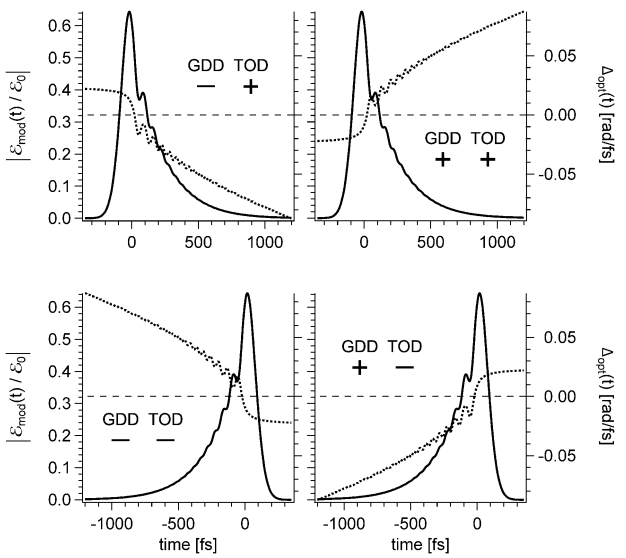

Fig. 1 Laser pulses, shaped by a combination of positive and negative GDD and TOD. Field amplitude (solid) and instantaneous optical detuning $\Delta_{\mathrm{opt}}(t) = \omega(t) - \omega_0$ (dotted) are plotted according to eqn (15). The maximum field amplitude of the bandwidth limited pulse corresponds to $\mathscr{E}_0$. Spectral phases of $\phi_2 = \pm 5000$ fs^2 and $\phi_3 = \pm 200\,000$ fs^3 are introduced. Gaussian shaped 800 nm pulses with a bandwidth limited pulse duration of 60 fs are used.

Table 1 Temporal properties of the field, *i.e.* $\mathscr{E}_{\mathrm{mod}}(t)$ and the instantaneous detuning $\Delta_{\mathrm{opt}}(t)$ for the four possible combinations of sign alternations of the *gerade* ($\pm\varphi_{\mathrm{g}}(\omega)$) and the *ungerade* ($\pm\varphi_{\mathrm{u}}(\omega)$) part of a phase modulation function $\varphi(\omega) = \varphi_{\mathrm{g}}(\omega) + \varphi_{\mathrm{u}}(\omega)$ exemplified by GDD and TOD. The ordering of the table entries is according to Fig. 1

	$-\varphi_{\mathrm{g}}(\omega)$	$\varphi_{\mathrm{g}}(\omega)$
$\varphi_{\mathrm{u}}(\omega)$	−GDD, +TOD $-\varphi(-\omega)$ $\mathscr{E}^*_{\mathrm{mod}}(t)$ $-\Delta_{\mathrm{opt}}(t)$	+GDD, +TOD $\varphi(\omega)$ $\mathscr{E}_{\mathrm{mod}}(t)$ $\Delta_{\mathrm{opt}}(t)$
$-\varphi_{\mathrm{u}}(\omega)$	−GDD, −TOD $-\varphi(\omega)$ $\mathscr{E}^*_{\mathrm{mod}}(-t)$ $\Delta_{\mathrm{opt}}(-t)$	+GDD, −TOD $\varphi(-\omega)$ $\mathscr{E}_{\mathrm{mod}}(-t)$ $-\Delta_{\mathrm{opt}}(-t)$

($\pm\varphi_{\mathrm{g}}(\omega)$) and *ungerade* ($\pm\varphi_{\mathrm{u}}(\omega)$) phase modulation functions analogous to the representation in Fig. 1. For the temporal properties we have assumed that the initially unmodulated field was real valued and symmetrical. For instance, a conjugation of the *gerade* part of the phase modulation function only, *i.e.* $\varphi_{\mathrm{g}}(\omega) \rightarrow -\varphi_{\mathrm{g}}(\omega)$ leaves the modulus of the envelope $|\mathscr{E}_{\mathrm{mod}}(t)|$ unchanged but inverts the detuning $\Delta_{\mathrm{opt}}(t) \rightarrow -\Delta_{\mathrm{opt}}(t)$. Likewise, conjugation of the *ungerade* part of the phase modulation function, *i.e.* $\varphi_{\mathrm{u}}(\omega) \rightarrow -\varphi_{\mathrm{u}}(\omega)$ leads to time reversal of the envelope $|\mathscr{E}_{\mathrm{mod}}(t)| \rightarrow |\mathscr{E}_{\mathrm{mod}}(-t)|$ and time reversal of the inverted detuning $\Delta_{\mathrm{opt}}(t) \rightarrow -\Delta_{\mathrm{opt}}(-t)$. Time reversal of both the envelope $|\mathscr{E}_{\mathrm{mod}}(t)| \rightarrow |\mathscr{E}_{\mathrm{mod}}(-t)|$ and

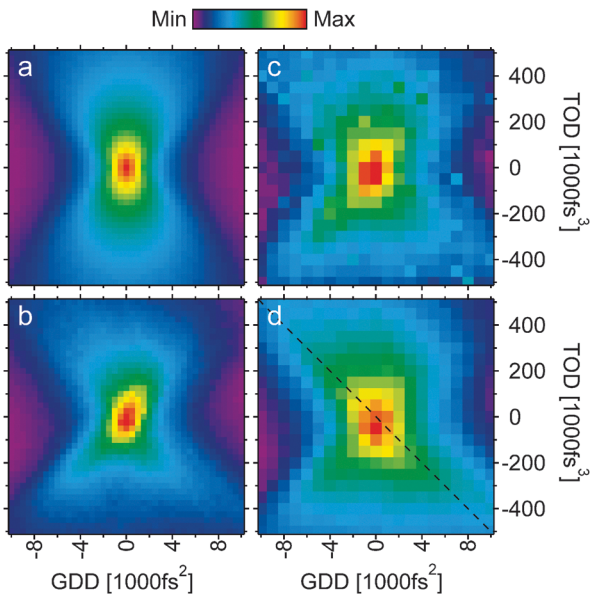

Fig. 2 Two-photon signals induced by GDD–TOD-modulated laser pulses. (a) Simulation of SHG for a Gaussian 60 fs pulse. (b) Measured fluorescence of DCM after two-photon absorption. (c) 510 nm fluorescence from porphyrazine **1**. (d) 710 nm fluorescence from **1** (pump power 1/4 $\bar{P}_0$). Landscapes (b) and (c) are directly showing the population of the two-photon excited electronic state of DCM and **1**. Deviations from the simulated landscape (a) are attributed to the laser spectrum. Landscape (d) should be equal to (c), instead not only relaxation from the two-photon excited electronic state but another small component is showing up intensifying the diagonal direction inside the plot as indicated (dashed).

the detuning $\Delta_{opt}(t) \rightarrow \Delta_{opt}(-t)$ is achieved by conjugation of both the *gerade* and the *ungerade* phase functions.

The way in which light–matter-interaction is affected by different combinations of GDD and TOD is presented by a two-dimensional control landscape.[41–43,85] As phase modulation does not affect linear processes, an example for Second Harmonic Generation (SHG) by those pulses is given in Fig. 2a. The corresponding signal is calculated by: $S_{SHG} \propto \int|\mathscr{E}_{mod}(\phi_2,\phi_3,t)|^4 dt$.

3. Experiment

3.1 Setup

The experimental setup is shown schematically in Fig. 3. The laser source, a Ti : Sa femtosecond high energy oscillator (60 fs, 800 nm, Femtosource Scientific XL, Femtolasers) yields high pulse energies at a repetition rate of 11 MHz, being capable of covering the strong-field regime with the advantage of high repetition rates. This for instance increases the signal to noise ratio in nonlinear microscopy or enables accumulative experiments, in which the pulse repetition rate must be higher than the decay rate of the studied system. Beam power is adjusted by an attenuator and monitored in front of the sample by a power meter.

The femtosecond laser pulses are modulated employing a home-built polarization pulse shaper, which is similar to the pulse shaper described elsewhere.[93] Our setup is based on a folded 4*f*-zero dispersion compressor equipped with 1840 lines per mm Volume Phase Holographic Gratings (Wasatch Photonics) and cylindrical focussing mirrors with a focal length of $f = 227$ mm. The 2×640 pixel Liquid Crystal-Spatial Light Modulator (Jenoptik SLM-S640d) in the Fourier plane of the 4*f*-setup contains two liquid crystal layers with preferential orientation axes at $\pm 45°$. This configuration allows for independent and simultaneous spectral phase modulation of two orthogonally polarized electric field components of the incident linearly polarized light. Either both phase and polarization or both phase and amplitude control of the pulses entering the shaper is provided by this layout. Each pixel of the modulator covers a wavelength interval of about 0.16 nm (at 800 nm). This spectral resolution results in a temporal window of more than 10 ps available for the generation of almost arbitrarily shaped optical waveforms.

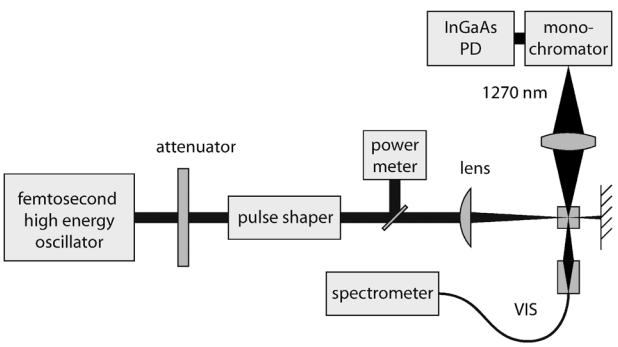

Fig. 3 Setup for 800 nm excitation of sensitizer dyes with shaped femtosecond laser pulses and detection of molecular luminescence signals in the visible and near-infrared range.

In the experiments discussed in this paper, we only make use of the phase modulation capabilities of the pulse shaper. Spectral phase-only modulation is realized by applying the same spectral phase functions to both liquid crystal arrays.

The beam is focused into a fluorescence cuvette (1×1 cm^2) by a lens ($f = 50$ mm). Typical peak intensities of bandwidth limited (BWL) pulses are approximated to $I = 60$ GW cm^{-2} while the sample is irradiated with an average power of $\bar{P}_0 = 64$ mW. Taking into account that dye molecules provide oscillator strengths in the range of unity, the pulse area $\int\Omega(t)dt = \mu/\hbar\int|\mathscr{E}(t)|dt$ reaches $4 \times 2\pi$ indicating strong-field excitation conditions. Luminescent light from a focal region smaller than the Rayleigh range of the beam is collimated into the fiber entrance of an imaging spectrograph (Oriel MS260i, cooled Andor CCD-Camera). A second detection pathway is used in order to measure weak signals in the near-infrared range (1270 nm) by an InGaAs photodiode.

3.2 Sensitizer dyes

The photosensitizer dye molecule under study (porphyrazine **1**) belongs to a class of tetrapyrrole dyes namely the quinoxalinodibenzo[*f*,*h*]porphyrazines. The chemical structure is shown in Fig. 4. Analytical data are provided in the ESI.† The synthesis will be described in detail elsewhere.

Molecules of porphyrazine **1** are dissolved in chloroform and optically characterized by the measurement of the absorption and fluorescence spectra with a spectrophotometer (Lambda 40, PerkinElmer) and luminescence spectrometer (LS-50B, PerkinElmer). Fresh samples show a characteristic Q-band ($S_0 \rightarrow S_1$) with an absorption maximum at 705 nm (Fig. 5). While adding an acid, *e.g.* gaseous HCl, to the sample, the appearance of a second absorption peak at 745 nm (Fig. 5) can be followed in the spectrum, originating from a second type of dye molecule (porphyrazine **2**) with a significantly red-shifted Q-band absorption maximum. At the same time the original Q-band signal of compound **1** is decreasing by an equal amount, indicating a conversion of the original molecules. Porphyrazine **1** can be reformed completely by restoring the pH-value with a base. We conclude that a monoprotonated analog[94] of **1** is formed by acidification.

This pH-dependence is utilized to prepare samples that include porphyrazines **1** and **2** simultaneously. By this approach both molecules are excited by the same laser pulses under identical experimental conditions. To exclude

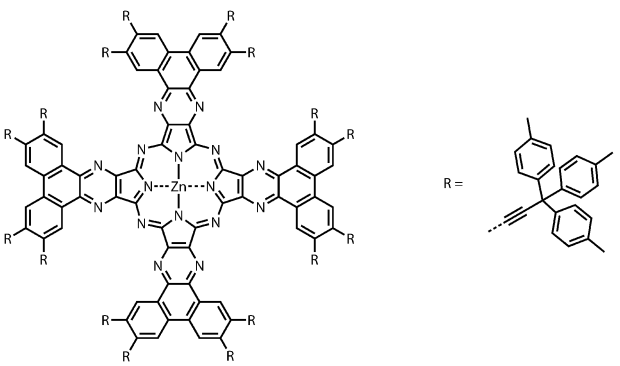

Fig. 4 Chemical structure of porphyrazine **1**.

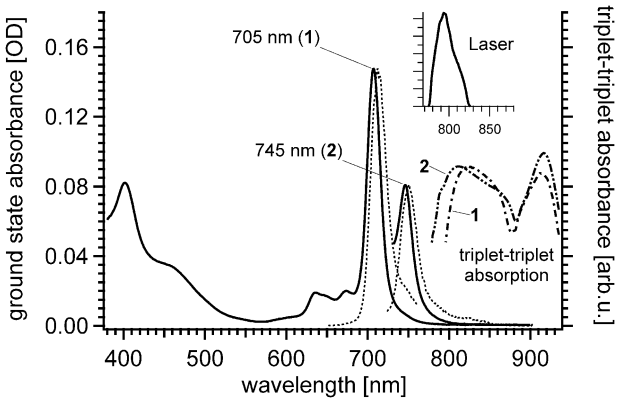

Fig. 5 Ground state absorption bands (— 705 nm/745 nm) and slightly stokes shifted fluorescence bands (--- 710 nm/750 nm) are shown for porphyrazine **1** and porphyrazine **2**. Note that fluorescence signals from the two molecules can be clearly distinguished, since the fluorescence bands are well-separated. Triplet state absorption bands of **1** (---) and **2** (·····) are measured upon excitation of the molecules in the corresponding Q-band.

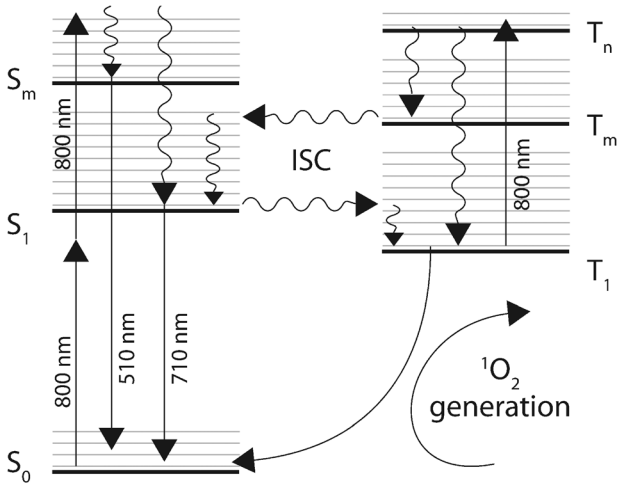

Fig. 6 Excitation scheme for porphyrazine **1** including excitation and relaxation processes in the singlet and triplet systems. Two-photon excitation in the singlet system is followed by fluorescence (510 nm, 710 nm) and ISC to the triplet system. One-photon excitation from T_1 enables a small part of population to return to the singlet system and show up in the 710 nm fluorescence signal. The scheme is also valid for porphyrazine **2** if level separations are adapted accordingly.

an influence of light-induced acid formation from chloroform, the UV/VIS spectrum of a sample is recorded before and after a measurement, ensuring that the concentrations of porphyrazines **1** and **2** remain constant.

3.3 Excitation scheme

In the course of the experiments we realized that direct strong-field excitation from the singlet ground state of sensitizer dyes with Q-bands at 800 nm suffers from severe photodegradation. For those sensitizers we observe bleaching of the fluorescence signal over longer excitation periods. Mass spectra (MALDI-TOF) of bleached samples show typical fragmentation of molecules into phthalimid derivatives with a quarter of the dyes mass.[95] Excitation with different pulse shapes results in different bleaching time constants, most likely making a multi-photon induced fragmentation responsible for the degradation process. Molecules that undergo fragmentation will show up in a signal loss. As the dependence of this loss of signal on GDD and TOD of shaped pulses is unknown, an extraction of underlying strong-field control of population transfer from measured signals is not feasible.

Instead, we use sensitizers without a one-photon absorption band at 800 nm and prepare those molecules in a new initial state in order to induce one-photon transitions. It was mentioned that sensitizer dyes undergo efficient intersystem crossing from the singlet to the triplet system after excitation. This is indicated by the high singlet oxygen quantum yield. Using high pulse repetition rates, molecules in the laser focus are accumulated in the triplet state T_1, since the life time of this state is long in comparison to the pulse separation. We noted that transitions between triplet states do not induce photo-degradation. Thus strong-field triplet–triplet transitions are studied with this approach.

An excitation diagram for porphyrazine **1** is shown schematically in Fig. 6. As the laser spectrum is centered at 800 nm with a bandwidth of about 30 nm, only two-photon excitation into a higher singlet state S_m is possible. Followed by fast relaxation processes, fluorescence from this singlet state (510 nm) as well as from the first excited singlet state S_1 (710 nm) occurs. Due to the two-photon character of the excitation process, the GDD–TOD landscapes for these fluorescence signals are expected to show an SHG-like dependence (as shown in Fig. 2a). Note that recently an enhancement of three photon absorption in iodine was observed by measuring GDD–TOD-landscapes.[85]

We now take into account that triplet accumulation occurs for higher fluences. Therefore triplet–triplet excitation must be considered in order to enter the strong-field regime. To that end the triplet–triplet absorption spectrum of porphyrazine **1** is measured using the spectrophotometer while pumping the sample in the Q-band by a band-pass filtered lamp. The ground state absorption spectrum is used as a base line. Characteristic bleaching of the ground state (705 nm) occurs with increasing pump power, accompanied by triplet absorption bands centered at 840 nm (T_n) and 915 nm (Fig. 5).

If the laser pulse encounters a triplet excited molecule, a nearly resonant one-photon transition into the T_n state is induced. After interaction with the laser pulse most of the population of this excited triplet state returns to the T_1 state by radiationless relaxation. However, as our measurement shows, a small part undergoes ISC to the singlet system, thus mapping the T_n state population onto the S_1 state and giving rise to additional fluorescence from the S_1 state. As triplet accumulation can be avoided by moving the sample, the triplet originating part of the fluorescence can be switched on and off consecutively. At the same time, fluorescence from S_m is not influenced by the ISC process and can serve as a reference. For high fluences and therefore triplet accumulation near saturation, the S_1 state population is influenced by two-photon excitation in the singlet state S_m on the one hand and T_n state mapping on the other hand to about the same amount. Since the dependence of the two-photon excitation on different pulse shapes (like ϕ_2–ϕ_3 variation) can be measured at 510 nm (Fig. 2c) and for

low fluences also at 710 nm (Fig. 2d), it can be subtracted from the overall fluorescence signal. Therefore information about the population transfer from T_1 to T_n can be extracted from the data.

To make sure that the average T_1 state population (average degree of triplet accumulation over seconds) is not influenced by pulse shaping and therefore T_1 defining a stable initial state, we also measure the singlet oxygen phosphorescence at 1270 nm (Fig. 3). Being induced by energy transfer from triplet excited sensitizer molecules, the singlet oxygen yield is proportional to the T_1 state population. Triplet state populations remain constant within variations of 2.5% for typical GDD–TOD landscapes. This confirms the assumptions of a small percentage of T_n population-mapping on S_1 and of a high degree of triplet accumulation. Therefore a stable initial state for excitation is prepared. We could also confirm a nearly constant T_1 state population by considering the excitation and relaxation processes described in Fig. 6 by modelling the sensitizer in terms of rate equations.

The photoinduced processes described for porphyrazine **1** here are also valid for porphyrazine **2**. In order to measure individual triplet–triplet absorption spectra for porphyrazine **1** and **2**, molecules are isolated in the presence of pyridine and HCl, respectively. While the Q-band of porphyrazine **2** is red-shifted from 705 nm to 745 nm in comparison to that of **1**, the triplet absorption band near 800 nm is blue-shifted by about 15 nm. Accordingly the detuning δ of the laser central frequency ω_0 with respect to the central triplet–triplet transition frequency ω_r is smaller for porphyrazine **2**.

3.4 Measurement

In order to compensate for an unwanted residual spectral phase being introduced by the laser source and optical elements in the beam path, the experimental setup is first used to *in situ* perform a feedback controlled phase compensation. An evolutionary algorithm is fed with the fluorescence signal of a two-photon absorbing dye molecule (DCM). As the same setup is used for the sensitizer dye experiments without readjustment, the optimal phase is valid for the position of interest, namely the focus position inside the sample cuvette. The quality of the phase compensation is checked by a GDD–TOD scan for the fluorescence of DCM which is shown in Fig. 2b. Using this method, deviations from a flat spectral phase are readily recognized, as comparison with frequency resolved optical gating pulse characterization revealed. The two-photon data are very sensitive to residual phases and the desired landscape for a flat phase can be simulated and must be symmetric to GDD = TOD = 0. Minor deviations from the exact shape of the calculated SHG-induced GDD–TOD landscape are attributed to the laser spectrum, which is not perfectly Gaussian.

The sensitizer dye is dissolved in chloroform setting the optical density of the cuvette to 0.15 at 705 nm. Then

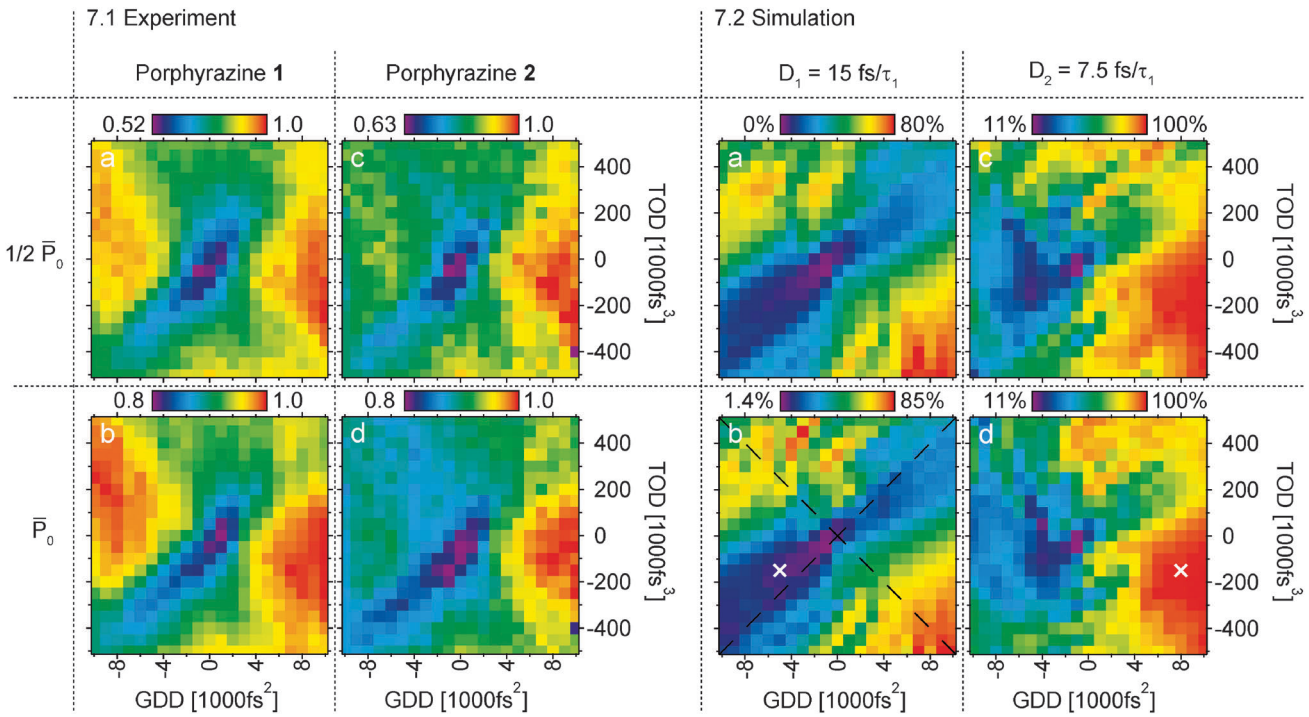

Fig. 7 Population transfer control landscapes for porphyrazine **1** (1a,1b) and porphyrazine **2** (1c,1d). Excitation power was chosen to be 1/2 $\bar{P}_0$ for (1a,1c) and $\bar{P}_0$ for (1b,1d). Fluorescence signals (710 nm, respectively, 750 nm) are plotted after subtraction of the two-photon induced signal contribution. Experimental data are compared to simulations with $D_1 = 15$ fs/τ_1 (2a,2b) and $D_2 = 7.5$ fs/τ_1 (2c,2d). Field amplitudes $\mathscr{E}_0$ (2a,2c) and $1.4\mathscr{E}_0$ (2b,2d) are used, corresponding to 1/2 $\bar{P}_0$ and $\bar{P}_0$ respectively. Landscapes show weak power dependence but are significantly different for the two detunings in both simulation (D_1 *vs.* D_2) and experiment (**1** *vs.* **2**). Comparison between corresponding landscapes from simulation and experiment (same character) shows good accordance in the main features. Markers in panels (2b) and (2d) indicate interesting regions of complete population return and population transfer as discussed in Section 5 in Fig. 13.

the pH-value is reduced until both porphyrazine **1** and porphyrazine **2** are present.

The absorption spectra before and after an experiment are recorded and found to match closely, indicating a very good photostability and constant density ratio of the molecules **1** and **2**. Effects such as thermal lensing, bubble formation or heating of the sample are not observed at our low optical densities. For several settings of the attenuator, *i.e.* laser intensities, GDD–TOD scans are performed recording the fluorescence of porphyrazine **1** at 710 nm and porphyrazine **2** at 750 nm at the same time. For low fluences only the two-photon absorption dependence shows up in the signals, as described above. This is depicted for porphyrazine **1** in Fig. 2d representatively (excitation power 1/4 $\bar{P}_0$). The two-photon induced reference signal at 510 nm shows the same behavior, as can be seen in Fig. 2c.

For higher fluences the shape of the pictures changes, indicating the onset of triplet originating fluorescence. (In Fig. 2d one might already identify a very weak enhancement in diagonal direction (dashed line) in comparison to Fig. 2c.) This part of the fluorescence is plotted in Fig. 7.1 for excitation at 1/2 $\bar{P}_0$ and $\bar{P}_0$, respectively, after having subtracted the two-photon contribution from the data. It is not possible to eliminate the two-photon contribution (about 50% of signal) experimentally in this excitation scheme, since the measured fluorescence signal indicates a relaxation to the singlet ground state, inevitably leading to two-photon excitation.

4. Simulation

The near-resonant transitions within the triplet system are simulated by numerical integration of the Time-Dependent Schrödinger Equation (TDSE) for a molecular two-state-system interacting with an intense, GDD–TOD-modulated femtosecond laser pulse. For generality, we model the system by two one-dimensional *harmonic* potentials $V_1(R)$ and $V_2(R)$, since harmonic potentials provide an appropriate approximation for a variety of molecules. As depicted in Fig. 8, the ground state electronic potential exhibits a stronger binding, resulting in a shorter vibrational oscillation period. The TDSE

$$i\hbar\frac{\partial}{\partial t}\Psi(R,t) = [\mathscr{T}(R) + \mathscr{V}(R,t)]\Psi(R,t) \qquad (18)$$

is solved iteratively by short-time propagation of the system state vector $\Psi = (\psi_1,\psi_2)^T$, employing a Fourier based split-operator method. Details of our procedure are given elsewhere.[3,96–98] In eqn (18), $\mathscr{T}(R)$ is the kinetic operator and $\mathscr{V}(R,t)$ is the potential operator including the interaction with the laser field. The interaction is treated in the dipole approximation. Making use of the rotating wave approximation in addition, the potential operator reads

$$\mathscr{V}(R,t) = \begin{pmatrix} V_1(R) & -\mu\mathscr{E}_{\mathrm{mod}}(t) \\ -\mu\mathscr{E}^*_{\mathrm{mod}}(t) & V_2(R) \end{pmatrix}, \qquad (19)$$

with μ being the transition dipole moment. The R-dependence of μ is suppressed for simplicity and, once again, to provide generality. Since we assume an oscillator strength of $f = 1$, the dipole moment is approximated correspondingly by $\mu = 4.4 \times 10^{-29}$ C m for an 800 nm transition. Modulated laser pulses follow eqn (7), utilizing a field amplitude of $\mathscr{E}_0 = 4.75 \times 10^6$ V cm^{-1} as a reference. This corresponds to 1/2 $\bar{P}_0$ and a BWL peak intensity of

$$I = \tfrac{1}{2}\varepsilon_0 c\mathscr{E}_0^2 = 30\ \mathrm{GW\ cm^{-2}}. \qquad (20)$$

In order to extend the applicability of our theoretical results even further, we generalize the molecular properties as well as the laser pulse parameters. To this end, we characterize light–matter-interaction by seven parameters, including the oscillation periods τ_1, τ_2 and the displacement Δr of the harmonic potentials, the molecular resonance frequency ω_r, the BWL pulse duration Δt, the field amplitude $\mathscr{E}_0$ and the relative pulse detuning $D = \delta/\omega_r$. As noted in Section 2, relative detuning can be introduced by shifting the laser central frequency, which is implemented in simulations instead of shifting potentials. The potential energy separation was chosen so that the molecular resonance lies at $\omega_r = 2.27$ rad fs^{-1} (830 nm), being within the triplet resonances of the porphyrazines **1** and **2**.

Note that equivalent GDD–TOD landscapes are obtained upon using different pulse durations Δt while at the same time scaling both the oscillation periods and the displacement of the potentials linearly and the detuning D reciprocally with Δt. Thus, we express all time parameters relative to the characteristic ground state vibrational period τ_1. Shorter vibrational periods are compensated by shorter pulse durations to establish the same physics within different molecules, if strong-field conditions are conserved ($\mu/\hbar\int|\mathscr{E}(t)|\,dt = 4 \times 2\pi$). To transform the GDD–TOD-modulated laser pulses to the new time scale, the GDD and TOD parameters are to be scaled with Δt^2 and Δt^3, respectively.

Fig. 9 shows the population transfer induced by GDD–TOD phase modulated laser pulses using the parameters from Fig. 8 and a pulse duration of $\Delta t = \tau_1/5$. The results from simulations with five different field amplitudes (Fig. 9a–e, $D = 15$ fs/τ_1) and five different detunings D (Fig. 9f–j, $\mathscr{E}_0$) are depicted. For the weak-field regime, represented by Fig. 9a with about 1.5% population transfer, the outcome of the excitation process is

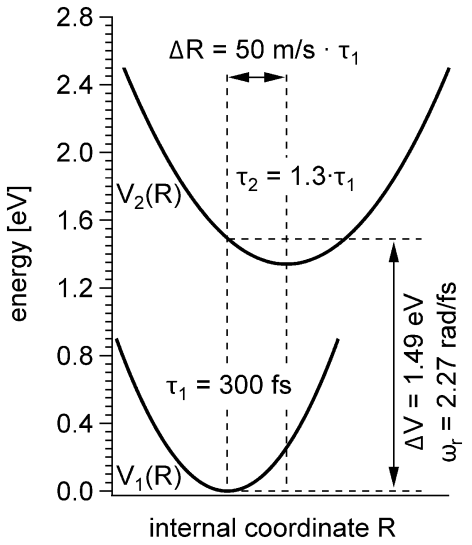

Fig. 8 Potential energy diagram as used for simulations.

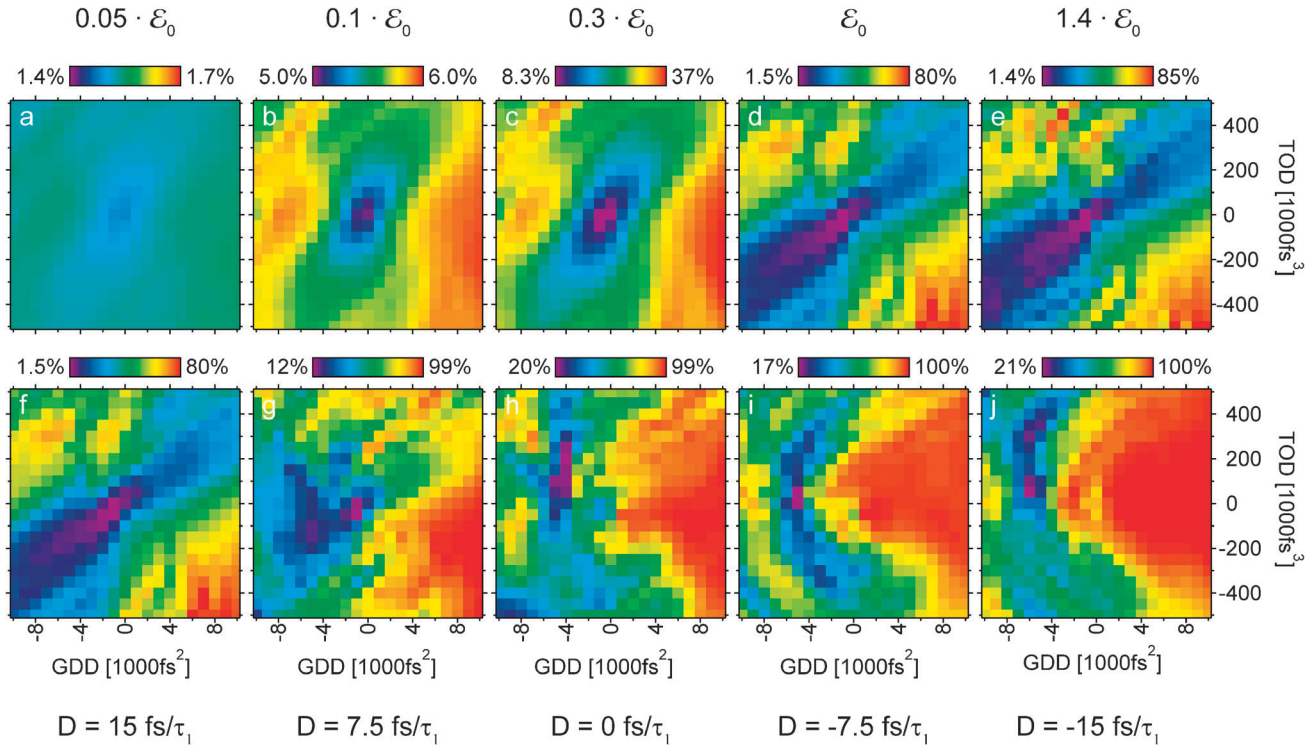

Fig. 9 Simulated population transfer for various field amplitudes (first row, $D = 15\ \mathrm{fs}/\tau_1$) and various detunings D (second row, field amplitude $\mathscr{E}_0$). While the landscape is flat in the weak-field limit (a), highly structured topologies arise for increasing field amplitude (b)–(e). The shape of the landscapes strongly depends on the relative detuning $D = \frac{\omega_0 - \omega_r}{\omega_r}$ of the laser central frequency ω_0 with respect to the molecular resonance frequency ω_r. Graphs (d) and (f) are identical.

nearly independent of the phase modulation, as to be expected for one-photon transitions. While increasing the field amplitude, reaching the strong-field regime (Fig. 9b–e), large areas of nearly complete population transfer and population return are gradually appearing. Beyond a threshold of about $\mathscr{E}_0$ (Fig. 9d) major parts of the control landscape become independent of the intensity, thus demonstrating robust and complete population transfer. Fig. 9f–j depict those robust control landscapes for detunings between $D = 15\ \mathrm{fs}/\tau_1$ and $D = -15\ \mathrm{fs}/\tau_1$.

Results for detuning parameters of $D_1 = 15\ \mathrm{fs}/\tau_1$ and $D_2 = 7.5\ \mathrm{fs}/\tau_1$ with field amplitudes of $\mathscr{E}_0$ and $1.4\mathscr{E}_0$ are compared with the experiment in Fig. 7.2, being assigned to the experimental data in Fig. 7.1.

4.1 Modeling the influence of decoherence

In order to account for decoherence effects of molecules in liquid solution, we introduce fluctuations in the quantum mechanical phase of the excited state wave function $\psi_2(R,t)$. As a result of the solvent surrounding the molecules, a transition process may suffer from a number of arbitrary phase shifts. A Gaussian distribution of phase values is used for this purpose, with a standard deviation of $\sigma_G = 0.05\pi$, meaning that the absolute values of 68% of the introduced phases are smaller than 0.16 rad. Typical values for electronic coherence decay in the liquid phase are in the order of 10 fs. This is why we introduce phase shifts every 5 fs. For each pulse shape we calculate the average value of 10 different arbitrary solvent surroundings, motivated by the fact that measurement involves averaging as well. Instead of extending the coherent model by phase kicks, more sophisticated methods to deal with decoherence are available, for instance the use of the density matrix formalism by solving Liouville's equation.

In general, our studies on decoherence introduced to the interaction process for various detunings D and field strengths (not shown) indicate that the effect of phase noise has—within reasonable limits—surprisingly little influence on the overall shape of the control landscape. As expected, strongly (spectrally) modulated and hence *long* pulses are more sensitive to decoherence effects than BWL pulses. Fig. 10 exemplarily shows a comparison of the measured landscape presented in Fig. 7.1b ($D = 5\%$, $\bar{P}_0$) to the corresponding simulation result displayed in Fig. 7.2b and Fig. 9e ($D_1 = 15\ \mathrm{fs}/\tau_1$, $1.4\mathscr{E}_0$) respectively. While Fig. 10b shows once more the coherent landscape, Fig. 10c shows the influence of phase noise with $\sigma_G = 0.05\pi$ on the same landscape achieving a substantial degree of accordance with the measurement. Only in the limit of very large σ_G values, *i.e.* essentially incoherent excitation conditions, the landscape topology is leveled out, as evident from Fig. 10d for $\sigma_G = 10\pi$. Thus, we conclude that the observed structures in both the measured and the simulated control landscape are due to *coherent* processes at play in the molecular strong-field excitation dynamics. Note in addition, that in the theoretical publication from Cao *et al.*,[68] where efficient population transfer is discussed in terms of vibrational coherence in the femtosecond regime and adiabatic passage in the picosecond regime, also the influence of thermal distributions and electronic dephasing has been investigated. A certain robustness of efficiency with respect to these parameters was found.

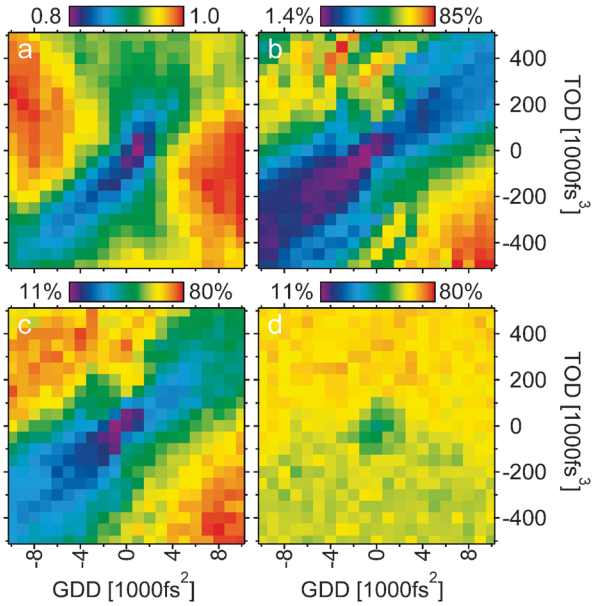

Fig. 10 Effect of decoherence on population transfer control landscapes. (a) Measurement. (b) Coherent simulation. (c) Decoherence: $\sigma_G = 0.05\pi$. (d) Decoherence: $\sigma_G = 10\pi$. The measured landscape (a) is in good accordance with simulations where moderate decoherence is included (c). In the limit of fast coherence decay (d) the landscape topology is leveled out.

Additionally we carried out a computational study comparing the coherence decay of atoms with that of an adequately chosen molecular system. The same decoherence model turns out to affect atomic population transfer more severely. In those simulations a set of two-level atoms with adequate detunings D account for the variety of possible transitions inside the molecular system. Unless these atomic systems are coupled to each other by a molecular kinetic operator $\mathscr{I}$, the above parameters of decoherence introduce more phase noise into the control landscapes. While new vibrational states get involved into transition processes by the $\mathscr{I}$-operator, the molecular system is less sensitive to decoherence. We conclude that the nuclear dynamics in the molecule diminishes the decoherence effect on population transfer when exciting the system in the strong-field regime. This might lead to more pronounced effects in the measurement of coherent signals if strong fields are applied.

5. Discussion

Even though based on simplifying assumptions, our simulations reproduce the main features of the experimental results. Especially the considerable differences between the measured landscapes of porphyrazine **1** and **2** are reproduced in the simulations. Markers in simulated landscapes Fig. 7.2b and 7.2d indicate regions of nearly complete population return and complete population transfer which are well-included as regions with high and low signals in the measured landscapes as well. Quantitative comparison of the population transfer efficiency between results from simulation and measurements is not directly possible. Averaging over the intensity distribution of our laser beam profile and the random orientation of molecules in solution inhibit the extraction of absolute numbers from the experiments. However there is indirect evidence for efficient population transfer—*i.e.* transfer of tens of percent up to 100% of ground state population—*via* comparison of simulated and measured data. The observed contrasts between maxima and minima of the measured landscapes are in the region of tens of percent, being in good agreement with contrasts obtained in our simulations when in addition averaging effects are considered.

The model system parameters that yield optimal accordance with the experiments are $D_1 = 5\%$, $D_2 = 2.5\%$, $\tau_1 = 300$ fs, $I = 30$ GW cm^{-2} and $I = 60$ GW cm^{-2}, respectively. We compare these values with the experimental conditions. The measured triplet–triplet absorption bands can be interpreted as mainly involving transitions at 840 nm (porphyrazine **1**) and 820 nm (porphyrazine **2**) with respect to a laser central wavelength at 800 nm. The resulting relative detunings are

$$\frac{\omega_0 - \omega_r}{\omega_r} = \frac{840\,\text{nm}}{800\,\text{nm}} - 1 = 5\% \text{ and } \frac{820\,\text{nm}}{800\,\text{nm}} - 1 = 2.5\%,$$

which equal D_1 and D_2, showing reasonable agreement of the relative detunings. The long vibrational period ($\tau_1 = 300$ fs) suggests that a large fraction of the sensitizer molecule is involved in the vibrational motion. Peak intensities I of the BWL laser pulses correspond to the experimental conditions ($1/2\ \bar{P}_0$ and $\bar{P}_0$).

5.1 Identification of control mechanisms

In the following analysis of the simulation results, we refer to the fully coherent case (*i.e.* do not account for coherence destroying effects), to obtain the most transparent picture of the involved time-dependent wave packet dynamics. A moderate loss of coherence was shown to have a minor effect on the shape of the resulting control landscapes, merely reducing the contrast of the data (see Fig. 10).

Considering BWL pulses in the strong-field regime, two kinds of pulse properties turn out to be of major importance for the wave packet dynamics in the model molecular system, that is the pulse duration Δt and the static detuning δ of the laser pulses. To highlight this aspect, we discuss the four cases of wave packet dynamics induced by a short pulse ($\Delta t = 0.2\tau_1$) and a long pulse ($\Delta t = 2\tau_1$) under both resonant and detuned conditions. In these limiting cases, the corresponding wave packet dynamics exhibit a distinct behavior.

The molecule is initially in the vibrationally cold electronic ground state, its wave function $\psi_0(R)$ being Gaussian shaped. The interaction of a pulse with an excited molecule will be considered later. In three of the four cases ($\Delta t = 0.2\tau_1$ resonant and detuned, $\Delta t = 2\tau_1$ detuned) we observe a wave packet coupling between ground and excited state wave packets if strong fields are applied. This coupling induces a Joint Motion (JOMO) of the wave packets. The effect is visualized in Fig. 11, where ground state and excited state wave packet propagation upon strong-field excitation is shown. The onset of the laser pulse creates a wave packet in the excited state, which subsequently starts to move on the potential energy curve. Thus, the internuclear distance increases along with its kinetic energy. Due to the continuing transitions between the electronic states, kinetic energy is

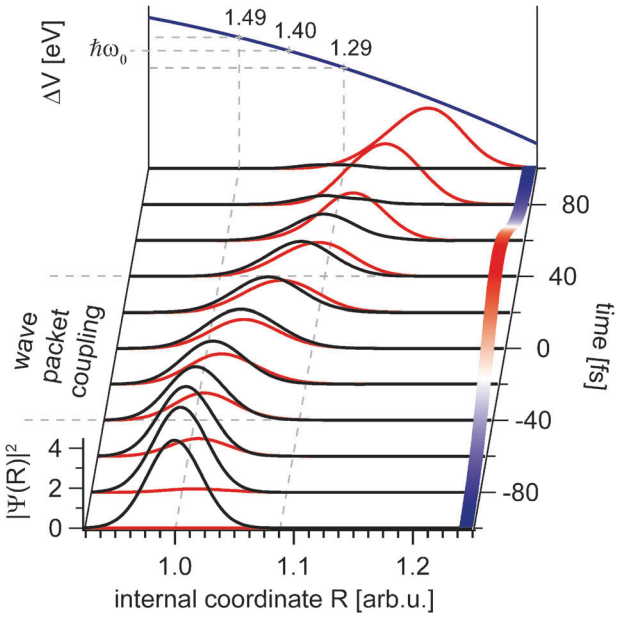

Fig. 11 (Video material available†) Illustration of joint wave packet motion induced by wave packet coupling. Propagation of wave packets upon strong-field excitation with a short pulse is depicted ($\Delta t = 1/5\tau_1$ and $D = -23$ fs/τ_1 corresponding to a 900 nm excitation with respect to the resonance at 830 nm). Ground state (black) and excited state wave packets (red) are depicted. The temporal field envelope of the pulse is shown on the right. Wave packets are coupled while a strong field is present and propagate to larger values of the internuclear distance R (JOMO). A potential difference value ΔV is assigned to the position $R(t)$ of the wave packets, reflecting the time dependent resonance of the molecule.

transferred to the electronic ground state and, consequently, a ground state wave packet is formed, being coupled to the excited state wave packet by the field. Both wave packets propagate concertedly (JOMO), until the field strength and hence the coupling decreases. Comparison between weak-field and strong-field excitation shows that JOMO slows down the propagation of the excited state wave packet.

In contrast to JOMO, the fourth case ($\Delta t = 2\tau_1$ resonant) induces completely different dynamics. Here, determined by the Franck–Condon factors, mainly a single vibrational eigenstate is excited in the upper electronic state, while the shape of the Gaussian wave function in the ground state basically remains unaltered.

Both, JOMO and the excitation of a single eigenstate have in common that the instantaneous resonance frequency $\omega_r(t)$ of the molecule is well-defined throughout the entire transition process. In the former case, $\Delta V = V_2(R) - V_1(R) = \hbar\omega_r$ determines $\omega_r(t)$, being dependent on the instantaneous position $R(t)$ of the wave packet. In the latter case $\omega_r(t) =$ const is the resonance frequency of the undisturbed molecule, similar to the weak-field limit. Therefore, in both cases the instantaneous detuning $\Delta(t) = \omega(t) - \omega_r(t)$ is well-defined and the transition process can be discussed in an atom-like picture—however with a time dependence of the atomic resonance frequency. Projecting robust population transfer in molecules based on chirped excitation back to atom-like pictures was also discussed in a theoretical contribution in terms of the imaginary part of the transition dipole moment multiplied by the field amplitude.[69]

Adiabatic processes such as RAP are usually discussed in terms of the instantaneous laser frequency $\omega(t)$ and the instantaneous resonance frequency $\omega_r(t)$.[44] These two functions are related to the bare or *diabatic* states of the system. In the adiabatic limit, curve crossings of the diabatic states, typically result in efficient population transfer, whereas transitions are inhibited for non-crossing and widely separated curves. In the non-adiabatic case, *i.e.* whenever the corresponding dressed or *adiabatic* states are close to each other, Rabi oscillations are likely to occur and the final population transfer strongly depends on the laser field amplitude. All of these cases are sketched in Fig. 12.

Fig. 12a refers to the short BWL pulse as discussed above (Fig. 11). As opposed to RAP with chirped laser pulses, here $\omega(t) =$ const and $\omega_r(t)$ decreases with time due to the molecular dynamics (JOMO) induced by the laser pulse. Such a situation is also found in Stark Chirped RAP (SCRAP) where the adiabatic transfer with a BWL pulse can be achieved by creating the effective frequency sweep not *via* molecular dynamics but *via* intensity. The static detuning δ is chosen such that initially $\omega_r(t) > \omega(t)$ and at some later time a crossing occurs. This pulse induces complete population transfer, demonstrated in Fig. 11, where the ground state wave packet (black) is nearly depleted after the interaction. The second case (Fig. 12b) is valid for the long, narrowband BWL resonant pulse ($\Delta t = 2\tau_1$) with both $\omega(t)$ and $\omega_r(t)$ being constant functions. Simulations confirm that the field amplitude determines the degree of population transfer. In Fig. 12c $\omega(t)$ is considered to have—introduced by pulse shaping—the same time dependence as $\omega_r(t)$. This case was not discussed before. Although the BWL pulse would induce population transfer, the phase modulated pulse maximizes curve separation by energetically following the JOMO of the wave packets.

We summarize that in the limits of very small as well as very large values of Δt and δ, the molecular wave packet dynamics induced by BWL pulses is determined by the combination of these two pulse parameters. Due to the induced wave packet dynamics the molecular resonance frequency exhibits a time dependence: $\omega_r(t) = \omega_r[R(t)]$. Whether or not population is transferred by a pulse is governed by $\omega_r(t)$ relative to $\omega(t)$, as interpreted in the framework of adiabatic pictures (Fig. 12). The function $\omega(t)$ itself can be shifted by the parameter δ as

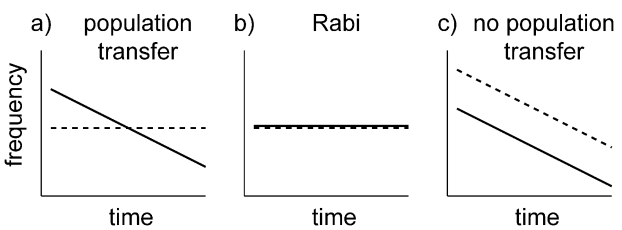

Fig. 12 Instantaneous molecular resonance frequency $\omega_r(t)$ (——) and instantaneous optical frequency $\omega(t)$ (---) for different static detunings δ, molecular dynamics and pulse shapes. (a) and (c) are examples of JOMO, (b) refers to the excitation of a vibrational eigenstate.

discussed above and is modulated in time for shaped pulses on the other hand, which will be considered next.

5.2 Assignment of control mechanisms to the GDD–TOD landscapes

We now analyze the light-induced dynamics with GDD–TOD pulses in terms of the above discussion. The GDD–TOD-modulated pulses under study provide both a slowly and fast varying part of the temporal envelope, if temporal pulse asymmetry is introduced by TOD (*cf.* Fig. 1). Wave packet dynamics for a slowly varying envelope is known from the long BWL pulses, while wave packet dynamics for the fast temporal envelope part refers to the short BWL pulse. Opposed to considerations based on BWL pulses, slow and fast envelope components come within *one* pulse, so that one part of the pulse prepares transient wave packets in the molecule and the second part no longer interacts with a molecule in the ground state. Both of those pulse parts are capable of modulating $\omega_r(t)$ in time, since specific wave packet dynamics is induced. The dynamic molecular resonance frequency $\omega_r(t)$ is combined with an instantaneous laser frequency $\omega(t)$, which is introduced by GDD. The GDD–TOD landscapes include four different combinations of envelope dynamics (fast → slow and slow → fast) and instantaneous frequency ($\omega(t) > \omega_0 \rightarrow \omega(t) < \omega_0$ and $\omega(t) < \omega_0 \rightarrow \omega(t) > \omega_0$), as shown in the examples from Fig. 1. Therefore very distinct cases of light–matter-interaction arise.

The dynamics is exemplified on characteristic regions of the landscapes, where complete population transfer or complete population return appears. The case of complete population return is discussed for a detuning of $D = 15\ \mathrm{fs}/\tau_1$ and a field amplitude of $1.4\mathscr{E}_0$ at the coordinates GDD = $-5000\ \mathrm{fs}^2$ and TOD = $-150\,000\ \mathrm{fs}^3$ (*cf.* Fig. 7.2b and 13a). The pulse starts with a slowly varying envelope and a significant instantaneous detuning $\Delta(t)$. Therefore wave packet coupling induces JOMO of the wave packets, allowing for an extraction of a well-defined internuclear distance $R(t)$ (center of mass of the excited state wave packet) and for an assignment of $\omega_r(t) = \omega_r[R(t)]$, which is depicted in Fig. 13a. Consequently, $\omega_r(t)$ decreases along with $\omega(t)$ as shown for JOMO in Fig. 11. The fast envelope part of the pulse continues JOMO until the field becomes too weak ($t = 150$ fs) and the coupling breaks up. Only transient population is transferred to the excited state and nearly complete population return occurs, since $\omega(t)$ and $\omega_r(t)$ are well separated at all times as depicted in the off-resonant case in Fig. 12c. (The drop of $\omega_r(t)$ at the end of the pulse is caused by the onset of free wave packet oscillation in the excited state potential after interaction with the laser pulse).

For $D = 7.5\ \mathrm{fs}/\tau_1$, again using a field amplitude of $1.4\mathscr{E}_0$, simulations indicate complete population transfer (*cf.* Fig. 7.2d and 13b). Representatively, we discuss a modulated pulse with GDD = $8000\ \mathrm{fs}^2$ and TOD = $-150\,000\ \mathrm{fs}^3$. Once more, the slow envelope part is first, but this time interaction is initiated near to the resonance. Thus, a vibrational eigenstate is populated by the first part of the pulse and $\omega_r(t)$ remains constant. The second part of the pulse starts while the molecule is mainly prepared in the transient vibrational eigenstate

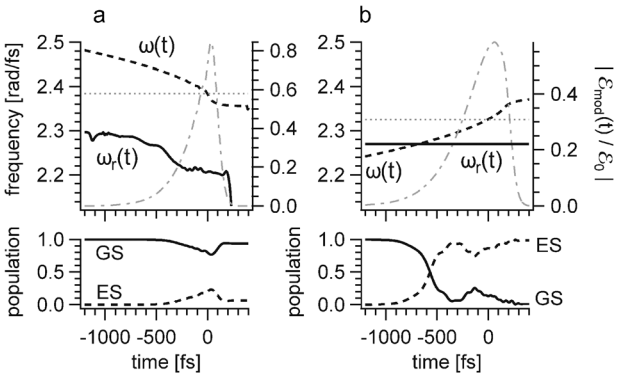

Fig. 13 (Video material available†) Nearly complete population return (a) and complete population transfer (b) induced by differently shaped laser pulses (GS = ground state, ES = excited state). The laser central frequency ω_0 (···) visualizes the static detuning of the laser from the Franck–Condon point at 2.27 rad fs^{-1} (*cf.* Fig. 8). (a) Non-crossing of the functions $\omega_r(t)$ (——) and $\omega(t)$ (---) is achieved by a following of the time-dependent molecular resonance ($\omega_r[R(t)]$ due to JOMO) *via* a decreasing $\omega(t)$ of the shaped pulse. The pulse parameters are $D = 15\ \mathrm{fs}/\tau_1$, $1.4\mathscr{E}_0$, GDD = $-5000\ \mathrm{fs}^2$ and TOD = $-150\,000\ \mathrm{fs}^3$ (Fig. 7.2b, marked). (b) The crossing occurs, because a vibrational eigenfunction is excited which keeps $\omega_r(t)$ constant, while $\omega(t)$ is tuned over the resonance. Complete population transfer is achieved by a pulse with $D = 7.5\ \mathrm{fs}/\tau_1$, $1.4\mathscr{E}_0$, GDD = $8000\ \mathrm{fs}^2$ and TOD = $-150\,000\ \mathrm{fs}^3$ (Fig. 7.2d, marked).

(population mainly in the excited state). Thus, wave packet coupling only generates a replica of the excited state wave function in the ground state without the transfer of kinetic energy as observed for JOMO. Transitions only occur at the Franck–Condon point and $\omega_r(t) = 2.27$ rad fs^{-1} describes a good approximation for the entire process. Fig. 13b contains a crossing of $\omega(t)$ and $\omega_r(t)$ similar to Fig. 12a, and hence, efficient population transfer occurs. Here, the laser frequency $\omega(t)$ is the time dependent function that induces the crossing and the transition process corresponds to RAP. Note that adiabatic interaction requires a reasonably smooth temporal envelope of the modulated pulses. This limits the GDD and TOD parameters to a range restricted by the constraint of large values for |GDD/TOD|. That part of the control landscapes is included in two triangular regions with vertices at (GDD;TOD) = (0;0), ($-10\,000\ \mathrm{fs}^2$; $-500\,000\ \mathrm{fs}^3$), ($-10\,000\ \mathrm{fs}^2$; $500\,000\ \mathrm{fs}^3$) and (0;0), ($10\,000\ \mathrm{fs}^2$; $-500\,000\ \mathrm{fs}^3$), ($10\,000\ \mathrm{fs}^2$; $500\,000\ \mathrm{fs}^3$), as indicated in Fig. 7.2b. Interestingly these regions of the control landscapes exhibit a smooth topology, whereas in other regions oscillating features occur.

6. Conclusions

Motivated by previous weak-field and strong-field experiments, we have designed laser pulses in order to study electronic population transfer in photosensitizer dyes in a strong-field experiment. Two dyes with different triplet absorption bands are prepared in the triplet ground state to examine population transfer by near-resonant transitions within the triplet system. Control landscapes with respect to population transfer show highly structured topologies which differ for the two sensitizer dyes under study and are robust over a certain range of applied laser intensities.

Experimental results are compared to simulations for a molecular two-state system, where for generality two parameterized one-dimensional harmonic potentials are considered. Calculated control landscapes based on the same pulse parameters are in good accordance with experimental data for both sensitizer dyes, while different detunings of the laser central frequency to the dye absorption bands are accounted for by appropriate detunings in simulations. We identify areas with complete population transfer and nearly complete population return inside the landscapes, both being robust over a wide range of intensity variations. Landscape topologies are leveled out completely in the incoherent limit of light–matter-interaction, thus coherent control is responsible for the effect in population transfer. Good accordance of measured and simulated landscapes implies that coherent control of population transfer in sensitizer dyes is demonstrated in the liquid phase, *i.e.* in the presence of decoherence.

We analyze the physical mechanisms controlling the final state populations in simulations and find that a combination of wave packet dynamics and adiabatic interaction with a shaped pulse with varying instantaneous frequency determines the outcome of the excitation process. In three out of four control scenarios, we find that atom-like interpretations of the interaction are possible due to a confinement of transition frequencies by specifically induced wave packet dynamics when strong fields are applied. Those wave packet dynamics are either characterized by a coupling of the ground state and excited state wave packets, inducing a joint wave packet motion and leading to a well-defined joint internuclear distance $R(t)$, or by exclusive excitation of a single vibrational eigenstate by narrowband interaction in the Franck–Condon region. The time-dependent molecular transition frequency induced by joint wave packet motion allows for efficient population transfer, if a BWL pulse with constant instantaneous laser frequency is used and a crossing of the two frequency curves occurs. A RAP-like process is observed if wave packet dynamics does not influence the transition frequency of the molecule (excitation of a vibrational eigenstate), while the instantaneous frequency of the laser is tuned over the molecular resonance.

Robust and efficient strong-field coherent control of population transfer is demonstrated experimentally for the first time to our knowledge in the liquid phase. Measuring GDD–TOD control landscapes gives us access to efficient population transfer *via* a wealth of mechanisms beyond the well-known pump–dump scheme. The effect was shown for sensitizer dyes, which play an important role in biological, chemical and medical applications which might directly profit from our findings, as a maximal sudden production of reactive singlet oxygen in cells and tissues could be achieved for instance. In addition other applications based on laser activated fluorescence dyes as for example nonlinear fluorescence microscopy below the diffraction limit might also profit from the demonstrated route to coherent and robust strong-field excitation.

Acknowledgements

We thank Jan Fleischhauer and Christian Burmester for supplying the porphyrazine dyes, Chris Meier (Toulouse), Volker Engel (Würzburg) and Christiane Koch (Kassel) for discussions and Dirk Guldi, Silke Wolfrum (Erlangen) for the measurement of transient absorption spectra. Financial support from the DFG, the FASTQUAST network and the Universitätsgesellschaft Kassel e.V. is gratefully acknowledged.

References

1 A. H. Zewail, *J. Phys. Chem.*, 2000, **104**, 5660–5694.
2 *Femtosecond Chemistry*, ed. J. Manz and L. Woeste, VCH, Weinheim, 1995.
3 S. A. Rice and M. Zhao, *Optical control of molecular dynamics*, Wiley, New York, 2000.
4 M. Shapiro and P. Brumer, *Principles of the Quantum Control of Molecular Processes*, John Wiley & Sons, Hoboken, New Jersey, 2003.
5 D. J. Tannor and S. A. Rice, *Adv. Chem. Phys.*, 1988, **70**, 441–523.
6 M. Shapiro and P. Brumer, *Int. Rev. Phys. Chem.*, 1994, **13**, 187–229.
7 T. Baumert, J. Helbing and G. Gerber, *Advances in Chemical Physics–Photochemistry: Chemical Reactions and their control on the Femtosecond Time Scale*, John Wiley & Sons, Inc., New York, 1996, pp. 47–77.
8 H. Rabitz, R. de Vivie-Riedle, M. Motzkus and K. Kompa, *Science*, 2000, **288**, 824–828.
9 M. Shapiro and P. Brumer, *Int. Rev. Phys. Chem.*, 2003, **66**, 859–942.
10 D. Goswami, *Phys. Rep.*, 2003, **374**, 385–481.
11 M. Dantus and V. V. Lozovoy, *Chem. Rev.*, 2004, **104**, 1813–1859.
12 V. Bonacic-Koutecky and R. Mitric, *Chem. Rev.*, 2005, **105**, 11–65.
13 T. Brixner, T. Pfeifer, G. Gerber, M. Wollenhaupt and T. Baumert, *Femtosecond Laser Spectroscopy*, Springer Verlag, 2005, pp. 225–266.
14 M. Wollenhaupt, V. Engel and T. Baumert, *Annu. Rev. Phys. Chem.*, 2005, **56**, 25–56.
15 P. Nuernberger, G. Vogt, T. Brixner and G. Gerber, *Phys. Chem. Chem. Phys.*, 2007, **9**, 2470–2497.
16 J. Werschnik and E. K. U. Gross, *J. Phys. B: At., Mol. Opt. Phys.*, 2007, **40**, R175–R211.
17 W. Wohlleben, T. Buckup, J. L. Herek and M. Motzkus, *ChemPhysChem*, 2007, **6**, 850–857.
18 Y. Silberberg, *Annu. Rev. Phys. Chem.*, 2009, **60**, 277–292.
19 K. Ohmori, *Annu. Rev. Phys. Chem.*, 2009, **60**, 487–511.
20 C. Brif, R. Chakrabarti and H. Rabitz, *New J. Phys.*, 2010, **12**, 075008.
21 R. Stoian, M. Wollenhaupt, T. Baumert and I. V. Hertel, *Laser precision microfabrication*, Springer, Berlin, 2010, vol. 135, pp. 121–144.
22 *Chemical Reactions and Their Control on the Femtosecond Time Scale – XXth Solvay Conference on Chemistry*, ed. P. Gaspard and I. Burghardt, John Wiley, New York, 1997.
23 J. L. Herek, *J. Photochem. Photobiol., A*, 2006, **180**, 225.
24 H. Fielding, M. Shapiro and T. Baumert, *J. Phys. B: At., Mol. Opt. Phys.*, 2008, **41**, 070201.
25 H. Rabitz, *New J. Phys.*, 2009, **11**, 105030.
26 A. M. Weiner, *Rev. Sci. Instrum.*, 2000, **71**, 1929–1960.
27 M. Wollenhaupt, A. Assion and T. Baumert, *Springer Handbook of Lasers and Optics*, Springer Science and Business Media, 2007, pp. 937–983.
28 D. B. Strasfeld, S. H. Shim and M. T. Zanni, *Adv. Chem. Phys.*, 2009, **141**, 1–28.
29 A. Monmayrant, S. Weber and B. Chatel, *J. Phys. B: At., Mol. Opt. Phys.*, 2010, **43**, 103001.
30 R. S. Judson and H. Rabitz, *Phys. Rev. Lett.*, 1992, **68**, 1500–1503.
31 T. Baumert, T. Brixner, V. Seyfried, M. Strehle and G. Gerber, *Appl. Phys. B: Lasers Opt.*, 1997, **65**, 779–782.
32 D. Meshulach, D. Yelin and Y. Silberberg, *Opt. Commun.*, 1997, **138**, 345–348.
33 C. J. Bardeen, V. V. Yakolev, K. R. Wilson, S. D. Carpenter, P. M. Weber and W. S. Warren, *Chem. Phys. Lett.*, 1997, **280**, 151–158.

34 A. Assion, T. Baumert, M. Bergt, T. Brixner, B. Kiefer, V. Seyfried, M. Strehle and G. Gerber, *Science*, 1998, **282**, 919–922.
35 R. J. Levis and H. A. Rabitz, *J. Phys. Chem. A*, 2002, **106**, 6427–6444.
36 C. Daniel, J. Full, L. Gonzáles, C. Lupulescu, J. Manz, A. Merli, S. Vajda and L. Wöste, *Science*, 2003, **299**, 536–539.
37 T. Hornung, R. Meier and M. Motzkus, *Chem. Phys. Lett.*, 2000, **326**, 445–453.
38 A. Bartelt, A. Lindinger, C. Lupulescu, S. Vajda and L. Wöste, *Phys. Chem. Chem. Phys.*, 2003, **5**, 3610–3615.
39 S. Fechner, F. Dimler, T. Brixner, G. Gerber and D. J. Tannor, *Opt. Express*, 2007, **15**, 15387–15401.
40 S. Ruetzel, C. Stolzenberger, S. Fechner, F. Dimler, T. Brixner and D. J. Tannor, *J. Chem. Phys.*, 2010, **133**, 164510.
41 M. Wollenhaupt, A. Präkelt, C. Sarpe-Tudoran, D. Liese and T. Baumert, *J. Mod. Opt.*, 2005, **52**, 2187–2195.
42 T. Bayer, M. Wollenhaupt and T. Baumert, *J. Phys. B: At., Mol. Opt. Phys.*, 2008, **41**, 074007.
43 H. A. Rabitz, M. M. Hsieh and C. M. Rosenthal, *Science*, 2004, **303**, 1998–2001.
44 N. V. Vitanov, T. Halfmann, B. W. Shore and K. Bergmann, *Annu. Rev. Phys. Chem.*, 2001, **52**, 763–809.
45 B. W. Shore, *Acta Phys. Slovaca*, 2008, **58**, 243–486.
46 J. S. Melinger, S. R. Gandhi, A. Hariharan, J. X. Tull and W. S. Warren, *Opt. Commun.*, 1992, **68**, 2000.
47 V. S. Malinovsky and J. L. Krause, *Eur. Phys. J. D*, 2001, **14**, 147–155.
48 I. R. Sola, J. Santamaria and V. S. Malinovsky, *Phys. Rev. A: At., Mol., Opt. Phys.*, 2000, **61**, 043413.
49 M. Krug, T. Bayer, M. Wollenhaupt, C. Sarpe-Tudoran, T. Baumert, S. S. Ivanov and N. V. Vitanov, *New J. Phys.*, 2009, **11**, 105051.
50 S. Zhdanovich, E. A. Shapiro, M. Shapiro, J. W. Hepburn and V. Milner, *Phys. Rev. Lett.*, 2008, **100**, 103004.
51 C. Trallero-Herrero, J. L. Cohen and T. Weinacht, *Phys. Rev. Lett.*, 2006, **96**, 063603.
52 M. Wollenhaupt, A. Assion, O. Bazhan, C. Horn, D. Liese, C. Sarpe-Tudoran, M. Winter and T. Baumert, *Phys. Rev. A: At., Mol., Opt. Phys.*, 2003, **68**, 015401.
53 M. Wollenhaupt, D. Liese, A. Präkelt, C. Sarpe-Tudoran and T. Baumert, *Chem. Phys. Lett.*, 2006, **419**, 184–190.
54 T. Bayer, M. Wollenhaupt, C. Sarpe-Tudoran and T. Baumert, *Phys. Rev. Lett.*, 2009, **102**, 023004.
55 M. Wollenhaupt, T. Bayer, N. V. Vitanov and T. Baumert, *Phys. Rev. A: At., Mol., Opt. Phys.*, 2010, **81**, 053422.
56 M. Wollenhaupt, A. Präkelt, C. Sarpe-Tudoran, D. Liese and T. Baumert, *Appl. Phys. B: Lasers Opt.*, 2006, **82**, 183–188.
57 J. H. Posthumus, *Rep. Prog. Phys.*, 2004, **67**, 623–665.
58 T. Frohnmeyer, M. Hofmann, M. Strehle and T. Baumert, *Chem. Phys. Lett.*, 1999, **312**, 447–454.
59 B. J. Sussman, D. Townsend, M. Y. Ivanov and A. Stolow, *Science*, 2006, **314**, 278–281.
60 T. Baumert, V. Engel, C. Meier and G. Gerber, *Chem. Phys. Lett.*, 1992, **200**, 488–494.
61 D. B. Strasfeld, S. H. Shim and M. T. Zanni, *Phys. Rev. Lett.*, 2007, **99**, 038102.
62 J. L. Herek, W. Wohlleben, R. Cogdell, D. Zeidler and M. Motzkus, *Nature*, 2002, **417**, 533–535.
63 G. Vogt, G. Krampert, P. Niklaus, P. Nuernberger and G. Gerber, *Phys. Rev. Lett.*, 2005, **94**, 068305.
64 V. I. Prokhorenko, A. M. Nagy, S. A. Waschuk, L. S. Brown, R. R. Birge and R. J. D. Miller, *Science*, 2006, **313**, 1257–1261.
65 T. Brixner, N. H. Damrauer, P. Niklaus and G. Gerber, *Nature*, 2001, **414**, 57–60.
66 M. Roth, L. Guyon, J. Roslund, V. Boutou, F. Courvoisier, J. P. Wolf and H. Rabitz, *Phys. Rev. Lett.*, 2009, **102**, 253001.
67 J. Petersen, R. Mitric, V. Bonacic-Koutecky, J. P. Wolf, J. Roslund and H. Rabitz, *Phys. Rev. Lett.*, 2010, **105**, 073003.
68 J. Cao, C. J. Bardeen and K. R. Wilson, *Phys. Rev. Lett.*, 1998, **80**, 1406–1409.
69 J. Vala and R. Kosloff, *Opt. Express*, 2001, **8**, 238–245.
70 C. Schweitzer and R. Schmidt, *Chem. Rev.*, 2003, **103**, 1685–1757.
71 C. S. Foote, *Active oxygen in chemistry*, Blackie Acad. & Professional, London, 1995, 1st edn, vol. 2.
72 I. J. MacDonald and T. J. Dougherty, *J. Porphyrins Phthalocyanines*, 2001, **5**, 105–129.
73 J. M. Dela Cruz, I. Pastirk, M. Comstock and M. Dantus, *Opt. Express*, 2004, **12**, 4144–4149.
74 K. E. Sheetz and J. Squier, *J. Appl. Phys.*, 2009, **105**, 051101.
75 J. González-Vázquez, I. R. Sola, J. Santamaria and V. S. Malinovsky, *Chem. Phys. Lett.*, 2006, **431**, 231–235.
76 D. Yang, J. Savolainen, A. Jafarpour, D. Sprunken, J. L. Herek and D. H. Kessel, *Proc. SPIE–Int. Soc. Opt. Eng.*, 2009, **7380**, 73806H.
77 P. Brumer and M. Shapiro, *Chem. Phys.*, 1989, **139**, 221–228.
78 D. Meshulach and Y. Silberberg, *Nature*, 1998, **396**, 239–242.
79 V. V. Lozovoy, I. Pastirk, A. Walowicz and M. Dantus, *J. Chem. Phys.*, 2003, **118**, 3187–3196.
80 A. Präkelt, M. Wollenhaupt, C. Sarpe-Tudoran and T. Baumert, *Phys. Rev. A: At., Mol., Opt. Phys.*, 2004, **70**, 063407.
81 M. Shapiro and P. Brumer, *J. Chem. Phys.*, 2010, **132**, 186101.
82 A. Assion, T. Baumert, J. Helbing, V. Seyfried and G. Gerber, *Chem. Phys. Lett.*, 1996, **259**, 488–494.
83 S. Gräfe and V. Engel, *J. Phys. B: At., Mol. Opt. Phys.*, 2005, **414**, 17–22.
84 S. Malkmus, R. Dürr, C. Sobotta, H. Pulvermacher, W. Zinth and M. Braun, *J. Phys. Chem. A*, 2005, **109**, 10488–10492.
85 N. T. Form, B. J. Whitaker and C. Meier, *J. Phys. B: At., Mol. Opt. Phys.*, 2008, **41**, 074011.
86 P. Marquetand, P. Nuernberger, T. Brixner and V. Engel, *J. Chem. Phys.*, 2008, **129**, 074303.
87 A. Wand, S. Kallush, O. Shoshanim, O. Bismuth, R. Kosloff and S. Ruhman, *Phys. Chem. Chem. Phys.*, 2010, **12**, 2149–2163.
88 C. J. Bardeen, Q. Wang and C. V. Shank, *Phys. Rev. Lett.*, 1995, **75**, 3410–3413.
89 G. Cerullo, C. J. Bardeen, Q. Wang and C. V. Shank, *Chem. Phys. Lett.*, 1996, **262**, 362–368.
90 L. Englert, B. Rethfeld, L. Haag, M. Wollenhaupt, C. Sarpe-Tudoran and T. Baumert, *Opt. Express*, 2007, **15**, 17855–17862.
91 C. Horn, M. Wollenhaupt, M. Krug, T. Baumert, R. de Nalda and L. Banares, *Phys. Rev. A: At., Mol., Opt. Phys.*, 2006, **73**, 031401.
92 O. Vallée and M. Soares, *Airy Functions and Applications to Physics*, Imperial College Press, London, 2010, 2nd edn.
93 M. Wollenhaupt, M. Krug, J. Köhler, T. Bayer, C. Sarpe-Tudoran and T. Baumert, *Appl. Phys. B: Lasers Opt.*, 2009, **95**, 245–259.
94 P. Petrik, P. Zimcik, K. Kopecky, Z. Musil, M. Miletin and V. Loukotova, *J. Porphyrins Phthalocyanines*, 2007, **11**, 487–495.
95 R. Bonnett and G. Martínez, *Tetrahedron*, 2001, **57**, 9513–9547.
96 M. D. Feit and J. A. Fleck, Jr, *J. Chem. Phys.*, 1983, **78**, 301–308.
97 R. Kosloff, *Annu. Rev. Phys. Chem.*, 1994, **45**, 145–178.
98 M. Wollenhaupt and T. Baumert, *J. Photochem. Photobiol., A*, 2006, **180**, 248–255.

